Surface galvanic formation of Co-OH on Birnessite and its catalytic activity for the oxygen evolution reaction

Yayun Pu,[1,2] Veronica Celorrio,[3] Jöerg M. Stockmann,[4] Oded Sobol,[4] Zongzhao Sun,[2] Wu Wang,[5] Matthew J. Lawrence,[1] Jörg Radnik,[4] Andrea E. Russell,[6] Vasile-Dan Hodoroaba,[4] Limin Huang[2*] and Paramaconi Rodriguez[1*]

[1]School of Chemistry, University of Birmingham, Edgbaston, Birmingham B15 2TT, UK.

[2]Department of Chemistry, Southern University of Science and Technology, No. 1088 Xueyuan Blvd, Shenzhen, Guangdong 518055, China.

[3]Diamond Light Source Ltd, Diamond House, Harwell Campus, Didcot OX11 0DE, UK.

[4] Bundesanstalt für Materialforschung und -prüfung (BAM), Division 6.1 Surface analysis and interfacial Chemistry, Unter den Eichen 44-46, 12203 Berlin, Germany

[5]Department of Physics, Southern University of Science and Technology, Shenzhen, Guangdong, China.

[6] School of Chemistry, University of Southampton, Highfield, Southampton, SO17 1BJ, UK.

[*]Corresponding author: P.B.Rodriguez@bham.ac.uk , huanglm@sustc.edu.cn.

Abstract

Low cost, high-efficient catalysts for water splitting can be potentially fulfilled by developing earth abundant metal oxides. In this work, surface galvanic formation of Co-OH on $K_{0.45}MnO_2$ (KMO) was achieved via the redox reaction of hydrated Co^{2+} with crystalline Mn^{4+}. The synthesis

method takes place at ambient temperature without using any surfactant agent or organic solvent, providing a clean, green route for the design of highly efficient catalysts. The redox reaction resulted in the formation of ultrathin Co-OH nanoflakes with high electrochemical surface area. X-ray adsorption spectroscopy (XAS) and X-ray photoelectron spectroscopy (XPS) analysis confirmed the changes in the oxidation state of the bulk and surface species on the Co-OH nanoflakes supported on the KMO. The effect of the anions, chloride, nitrate and sulfate, on the preparation of the catalyst was evaluated by electrochemical and spectrochemical means. XPS and Time of flight secondary ion mass spectrometry (ToF-SIMS) analysis demonstrated that the layer of CoO_xH_y deposited on the KMO and its electronic structure strongly depends on the anion of the precursor used during the synthesis of the catalyst. In particular, it was found that Cl favors the formation of Co-OH, changing the rate determining step of the reaction, which enhances the catalytic activity towards the OER, producing the most active OER catalyst in alkaline media.

Key words: oxygen evolution reaction, surface galvanic synthesis, layered manganese oxide, anion effect.

1. Introduction

Electrochemical oxygen evolution reaction (OER) is one of the most extensively studied reactions in the last 10 years given its importance in the development of water splitting and hydrogen storage technologies.[1-5] Since the OER is a complex four-electron transfer reaction with slow kinetics, the development of highly active electrocatalysts is paramount to improve the efficiency of water electrolyzers. The Ru and Ir oxides are, so far, the most active materials for the OER, however the low abundance and consequently the high cost made the implementation of these materials in broadly use technologies, impervious.[6, 7] Due to the abundance and cost limitation, the use of other transition metal oxide (TMO) catalysts, such as Mn, Co and Ni based oxide catalysts have been subject of extensive studies.[8] To our knowledge, the first to report the kinetics of electrode oxygen evolution was Bockris,[9] and then other TMOs such as spinels, perovskites and hydroxides have been widely studied.[10-14] Over the recent years, these investigations have revealed the formation of surface oxo-hydroxide as the active species for the OER with turnover frequencies (TOF) up to 20 times higher than the oxide counterpart.[15-18] Besides all the efforts, one of the main limitations of metal oxide-based catalysts is the low number of active sites exposed on the surface. Such limitation is directly linked to the morphology of the catalyst and the preparation methods of the catalyst such electrodeposition,[19] co-precipitation,[20] cathodic corrosion,[21] and impregnation-annealing.[22] To fulfil the goal of exposing more active sites, tailoring surface chemistry is a feasible strategy.

Sorption of metal ions on manganese oxides from soils and rocks has long been known, especially on layered birnessite which consists of $Mn^{\delta+}$ ions (δ = Mn^{4+}, Mn^{3+}, Mn^{2+}).[23, 24] Inspired by the interaction between the transition metal ions with the layered manganese oxides, highly active catalysts can be developed.[25-27] For example, our recent work reported a highly

efficient OER catalyst by intercalation of Ni^{2+} into $K_{0.45}MnO_2$ (KMO) via ion exchange. Our previous work demonstrated that Mn^{3+} ions in KMO have an essential role in the ion intercalation and that the valence of hydrated $Ni(H_2O)_n^{2+}$ ions with d^8 subshell remains unchanged during the intercalation.[27]

In this work, we have taken advantage of the stronger reduction ability of hydrated $Co(H_2O)_n^{2+}$ ions (d^7) to promote the surface redox reaction with Mn^{4+} in KMO nanoparticles to form Co oxohydroxides (**Fig. 1**). The oxidation state and coordination of Co on KMO was analyzed by X-ray absorption spectroscopy (XAS) and X-ray photoelectron spectroscopy (XPS) in order to understand the catalytic activity towards the OER. Moreover, we report on the effect of the anion, chloride, nitrate and sulfate, during the catalyst preparation as well as their effect on the catalytic activity.

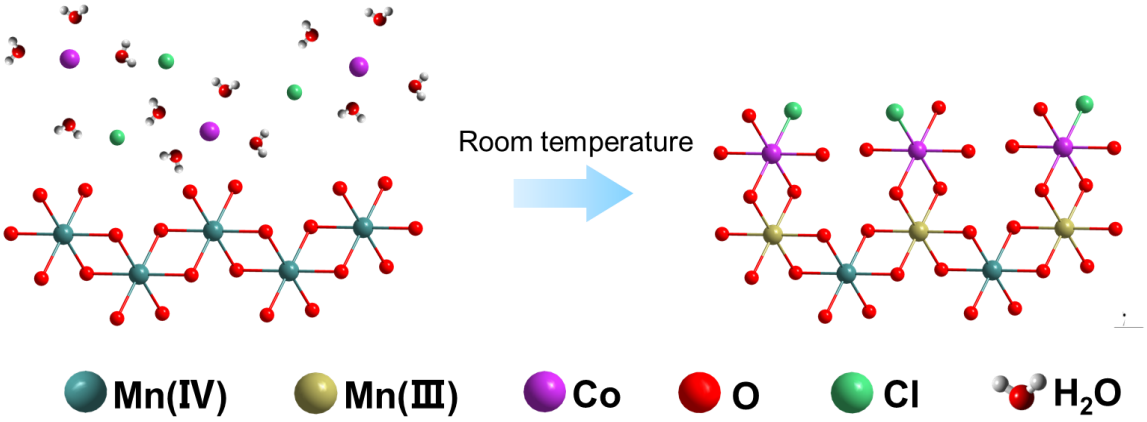

Figure 1. Schematic graph of hydrated Co^{2+} reacting with crystalline Mn^{4+} at room temperature.

2. Results and discussion

2.1 Synthesis and characterization of Co@KMO-Cl

Co@KMO samples were prepared by mixing synthesized K-rich Birnessite ($K_{0.45}MnO_2$) with different Co salt solutions at ambient temperature (details of the synthesis are given in the SI). The morphology and chemical analysis of the products by electron microscopy are shown in **Fig. 2**.

Scanning electron microscopy (SEM) images show the Co@KMO-Cl nanoparticles prepared using 0.5 M $CoCl_2$ as a precursor in **Fig. 2a**. Distinct differences in the morphology can be found compared to pristine KMO nanoparticles (**Fig. S1)**. In contrast to the flat and smooth surface of KMO, the Co@KMO-Cl nanoflakes show a surface densely covered with a porous structure (Fig. 2b). The EDS spectrum in **Fig. 2c,** confirms the incorporation of a significant amount of Co into the KMO framework. High-resolution transmission electron microscopy (HR-TEM) and high-angle annular dark field scanning transmission electron microscopy (HAADF-STEM) confirmed the formation of poorly-crystalline CoOOH nanoflakes at the interface of the layered-structure KMO (**Fig. 2d and e**). In order to try to address such concern, we have performed TEM measurements on Co@KMO-Cl nanoparticles as a function of time, in which the regions of the sample rich on CoOOH were exposed to the electron beam (dose rate: ~500 e/$Å^2$/s), the images were recorded in different intervals of time for 50 s. If the lattice fringes are induced by the electron beam, it would be expected to observe changes on the lattice as a function of time. Figure R1 shows the representative images after 1 s, 10 s, 20 s, 30 s, 40 s and 50 s. The lattice fringes of the COOH are indicated with yellow circles in the figure. As can be seen, the *"crystalline"* structure of the CoOOH nanoflakes remain unchanged during the 50 s of exposure to the electron beam of the TEM, thus we believe that the crystallization is not beam induced. To exclude the possibility of electron beam induced lattice fringe observed in the **Fig. 2f**, consecutive exposure of Co@KMO-Cl nanoparticles under electron beam was performed to confirmed the poor crystallinity nature of CoOOH nanoflakes (**Fig. S2**). The elemental distribution of Co, O, Mn, shown in **Fig. 2g,** unambiguously demonstrates the layered KMO support being coated by a Co-OH shell. Noteworthy is the heterogeneous distribution of Cl on the Co@KMO-Cl nanoparticles. Further discussion of the presence of chloride is presented later in the manuscript.

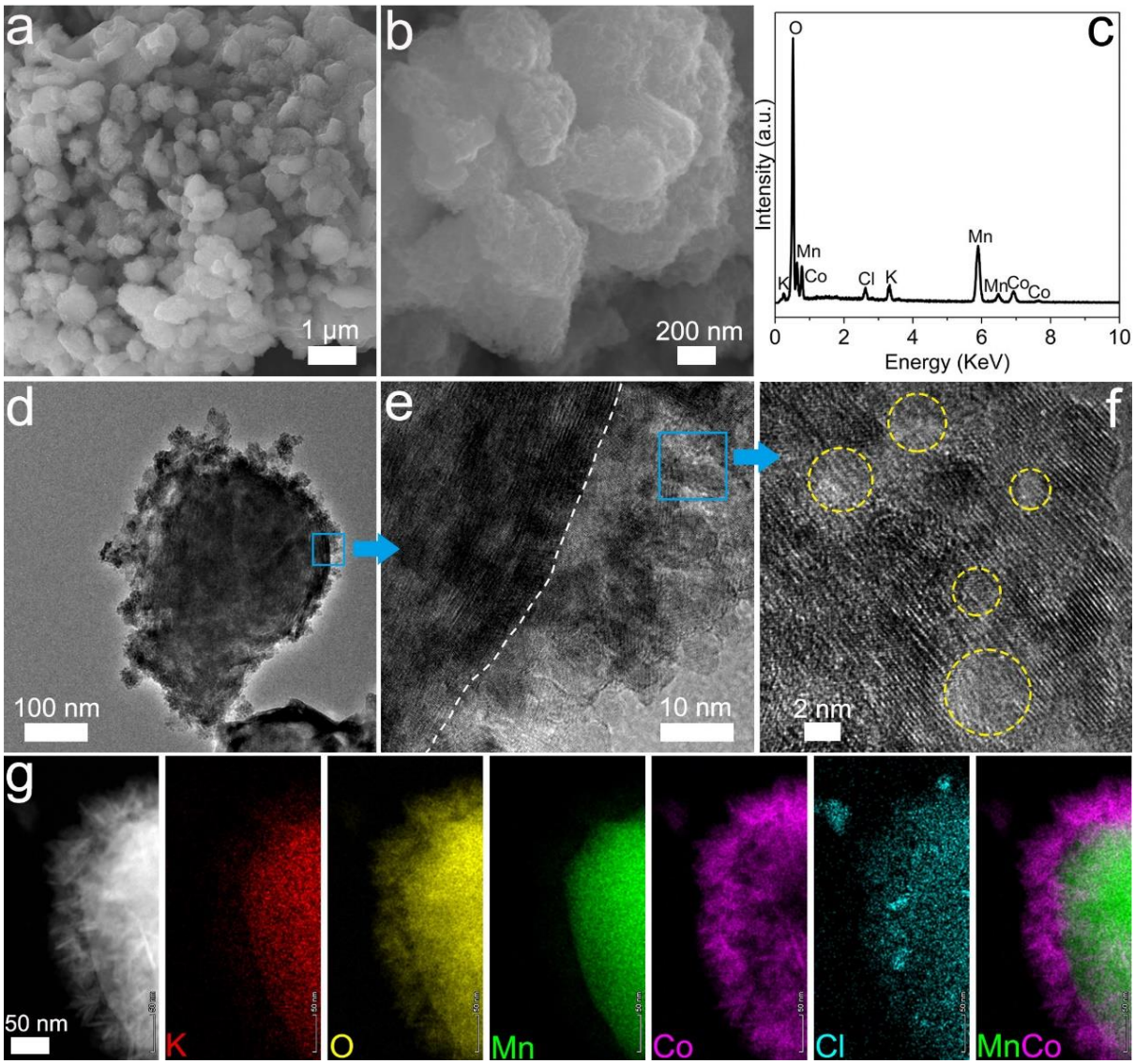

Figure 2. (**a**) (**b**) SEM images, (**c**) EDS, (**d-e**) TEM images of Co@KMO-Cl nanoplates. (**f**) enlarged area of COOH on the surface of Co@KMO-Cl, (**g**) HAADF-STEM image of a Co@KMO-Cl nanoplate with corresponding EDS elemental mapping.

In order to gain a better insight of the details of the structure and chemical composition of the Co@KMO-Cl nanoplates, X-ray diffraction (XRD), Raman spectroscopy, time-of-flight secondary ion mass spectrometry (ToF-SIMS) and X-ray absorption spectroscopy (XAS) were performed. XRD patterns in **Fig. 3a** show that the layered structure of Co@KMO-Cl retained the peaks at 12.4° and 24.8° associated to the (001) and (002) planes of KMO (monoclinic structure with *C*2/*m* space

group). However, their intensities were significantly weakened when compared to the pristine KMO, suggesting a reduced degree of crystallinity. **Fig. 3b** shows the comparison between the Raman spectra of pristine KMO and Co@KMO-Cl (**Fig. S3**). The fingerprint signals at 634 cm^{-1} and 578 cm^{-1} (A_g modes) are associated with the typical layered structure of Mn oxides. The signal at 634 cm^{-1} corresponds to out-of-plane Mn-O stretching vibrations perpendicular to the layers and the signal at 578 cm^{-1} corresponds to in-plane Mn-O vibration along the layers.[28-30] With surface modification of Co-OH species, the Raman spectra of the Co@KMO-Cl show a red shift of 14 cm^{-1} at 564 cm^{-1} and a blue shift of 22 cm^{-1} at 656 cm^{-1}, as well as a reduced intensity and broadened band width. In addition, the bands observed for KMO at wavenumbers lower than 450 cm^{-1} disappeared after the surface modification with Co. Pure CoOOH commonly present two peaks at 503 and 635 cm^{-1}[31, 32], which are perfectly overlapped with the KMO signals. The Raman spectra of Co@KMO-Cl is a combination of signals associated to CoOOH (503 cm^{-1} and 635 cm^{-1}) attributed to pristine CoOOH and the signals of distorted KMO (564 cm^{-1} and 656 cm^{-1}). These results are in agreement with the observations of the XRD patterns indicating the layered features of KMO were significantly weakened due to Co-OH species formation.

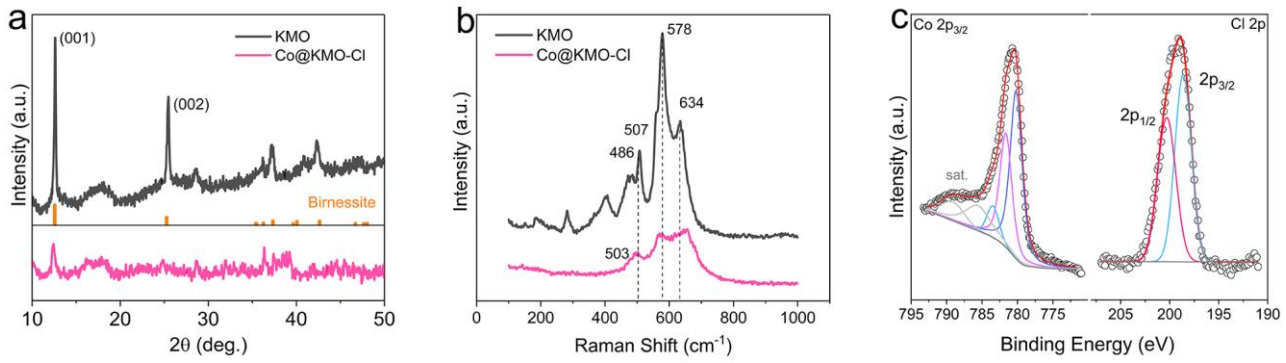

Figure 3. (**a**) X-ray diffraction patterns, **(b)** Raman spectra of pristine KMO and Co@KMO-Cl, (**c**) X-ray photoelectron spectra of Co@KMO-Cl with fit, left Co $2p_{3/2}$, right Cl 2p.

XPS and XAS were performed to probe the electronic environments of Co@KMO-Cl. The Co

$2p_{3/2}$ and Cl 2p XPS spectra and fits to the data are shown in **Fig. 3c**. The coexistence of bivalent and trivalent Co is indicated by deconvolution as well as the satellite features (at 785-793 eV). Detailed analysis is presented in below. Moreover, the Cl 2p detail spectrum shows the binding energy of $2p_{3/2}$ at 198.8 eV and $2p_{1/2}$ at 200.4 eV, with $\Delta E = 1.6$ eV, which can be assigned to a typical lattice Cl bonding with metal atom instead of adsorbed or interlayer Cl species at 198.0 eV.[33, 34] This observation was also supported by ToF-SIMS 3D reconstructed elemental distribution within the Co@KMO-Cl system (**Fig. 5a**). As can be observed, during sputtering of the nanostructure the signals of the Co and Cl species appear to be homogeneously distributed in the same x-y plane. The combination of the STEM-EDS (**Fig. 2g**), XPS, and ToF-SIMS suggests the presence of a strong chemical bond O···Co···Cl on the Co@KMO-Cl.

The changes of the electronic structure and oxidation state were evaluated by XAS. **Fig. 4a** shows the XANES spectra at the Co K-edge for Co@KMO-Cl and the oxides, which were used as standard reference compounds. A linear correlation between the K-edge edge position (defined as the maximum of the first derivative) and the metal oxidation state was previously established.[35] The average Co valence of Co@KMO-Cl was estimated to be 2.75+ (**Fig. S4**). **Fig. 4b** shows the spectra collected at the Mn K-edge, and the comparison with the pristine KMO. In this case, the analysis is significantly more complex due to the wide pre-edge feature (inset of **Fig. 4b**) and the influence of Mn coordination on the main edge.[36-38] For this reason, we performed X-ray emission spectroscopy (XES) characterization to determine quantitatively the ratios of $Mn^{2+}/Mn^{3+}/Mn^{4+}$ in KMO before and after the Co incorporation (**Fig. S5** and **Table S1**). The results indicate that 78% of the Mn^{4+} ions in KMO were converted to Mn^{3+}, leading to a clear decrease of mean oxidation state of Mn from 3.9+ on KMO to 3.1+ on Co@KMO-Cl. This change of the reduced Mn^{4+} is consistent with the percentage of oxidized Co^{2+} and demonstrates the proposed

reaction pathway in **Eq. (1)**:

$$\delta Co^{2+}{}_{(liq.)} + Mn^{4+}{}_{(cryst.)} \rightarrow \delta Co^{3+}{}_{(cryst.)} + Mn^{(4-\delta)+}{}_{(cryst.)} \qquad (0 < \delta < 1) \qquad (1)$$

The Co K-edge EXAFS Fourier transform (FT) of Co@KMO-Cl and reference samples are shown in **Fig. 4c**. The first peak at around 1.50 Å (not phased shift corrected) can be assigned to the first coordination shell Co–O, whereas the second peak at 2.50 Å is due to Co–Co and Co–Mn scattering (**Fig. S6** and **Table S2**). **Fig. 4d** shows the FT of the synthetized Co@KMO-Cl and KMO samples collected at the Mn edge, as well as the reference compounds. The first peak at ~1.5 Å (not phase shift corrected) is due to the Mn-O scattering and the second peak at ~ 2.5 Å (not phase shift corrected) is due to Mn-Mn and Mn-Co scattering (**Fig. S7 and S8** and **Table S3 and S4**). Nearly identical distances between Mn and its closest neighbor atoms for Co@KMO-Cl and KMO demonstrate the local coordination environment of Mn is largely maintained in the bulk. The Co-Mn redox reaction did not erase the KMO structure, consistent with the HRTEM image in **Fig. 2e** but induced point defects in the lattice that lead to the loss of crystallinity, as confirmed by the XRD results.

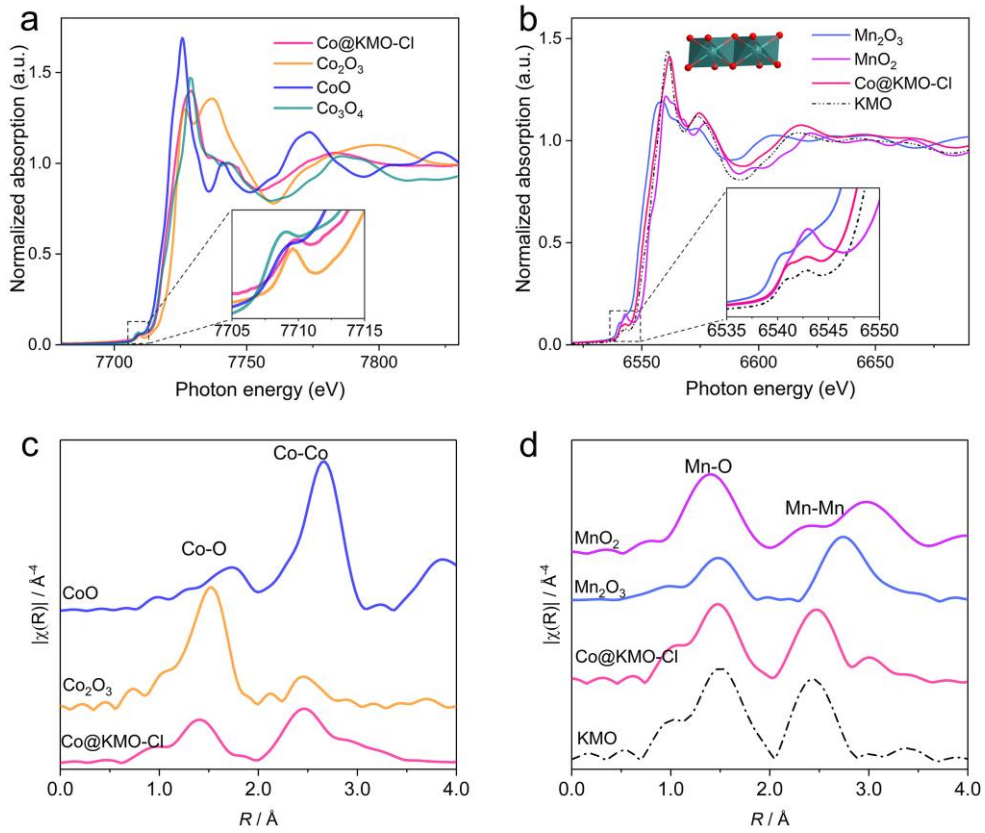

Figure 4. Normalized XANES spectra at the (**a**) Co K-edge, (**b**) Mn K-edge of the synthetized electrocatalysts. Spectra for reference compounds have been included as a comparison. Insets show the pre-edge region. Structure in **Fig. 4b** represents the structure of edge shared M-O octahedra from KMO where the red atoms are O, the dark blue atoms are Mn. EXAFS FTs of $k^3\chi(k)$ functions for the materials from Fig. 4a at the (**c**) Co K-edge, and (**d**) Mn K-edge.

2.2 Effect of the anions on morphology and electronic structure of Co@KMOs

We extended the investigation to the preparation of Co@KMO to explore the effects of the anion, examining both $(NO_3)^-$ and $(SO_4)^{2-}$, denoted as Co@KMO-NO and Co@KMO-SO.

The SEM and TEM images of Co@KMO-NO and Co@KMO-SO show similar morphologies to Co@KMO-Cl with the main feature as the formation of densely packed ultrathin Co-OH nanoflakes on the surface of the KMO nanoparticles (**Fig. S9)**. The EDS in **Fig. S9g-h** and XRF spectra in **Fig. S10** confirmed the incorporation of Co into the KMO particles. Interestingly, the signals associated

to S or N elements on the Co@KMO-NO and Co@KMO-SO were absent in both the XRF and EDS**,** in contrast to the observation of a considerable contribution of Cl in the spectra of the Co@KMO-Cl. Since the sensitivity of nonmetal on XPS is better than the XRF/EDS techniques, fairly weak N and S signals were detected in **Fig. S12f**, which contrast to the sharp peak of Cl. The XRF, EDS and XPS deliver consistent results, although slight difference due to the measuring resolution.

The presence or absence of the anions in the catalyst was further evaluated by ToF-SIMS 3D reconstruction (**Fig. 5A**). As can be seen in the ToF-SIMS depth profiles (**Fig. 5B**), the Co-O is the dominant etched species in the three catalysts. With regards to the Co-anion species, the spectra indicate coordination of the Co-Cl and Co-NO_3 in the corresponding catalysts. However, the correlation of Co to SO_4 species is very poor. On the other hand, the signal of the SO_4 is significant when detected as $MnSO_4$. These results suggest a stronger interaction of Cl^- and NO_3^{-1} with Co, while the SO_4^{-2} is interacting more strongly with Mn rather than with Co. It should be noted that the sensitivity of XPS/ToF SIMS is higher than the sensitivity of XRF and EDS.. Therefore, XPS/ToF SIMS provide more accurate information of anions Cl, N, S than the XRF and EDS.

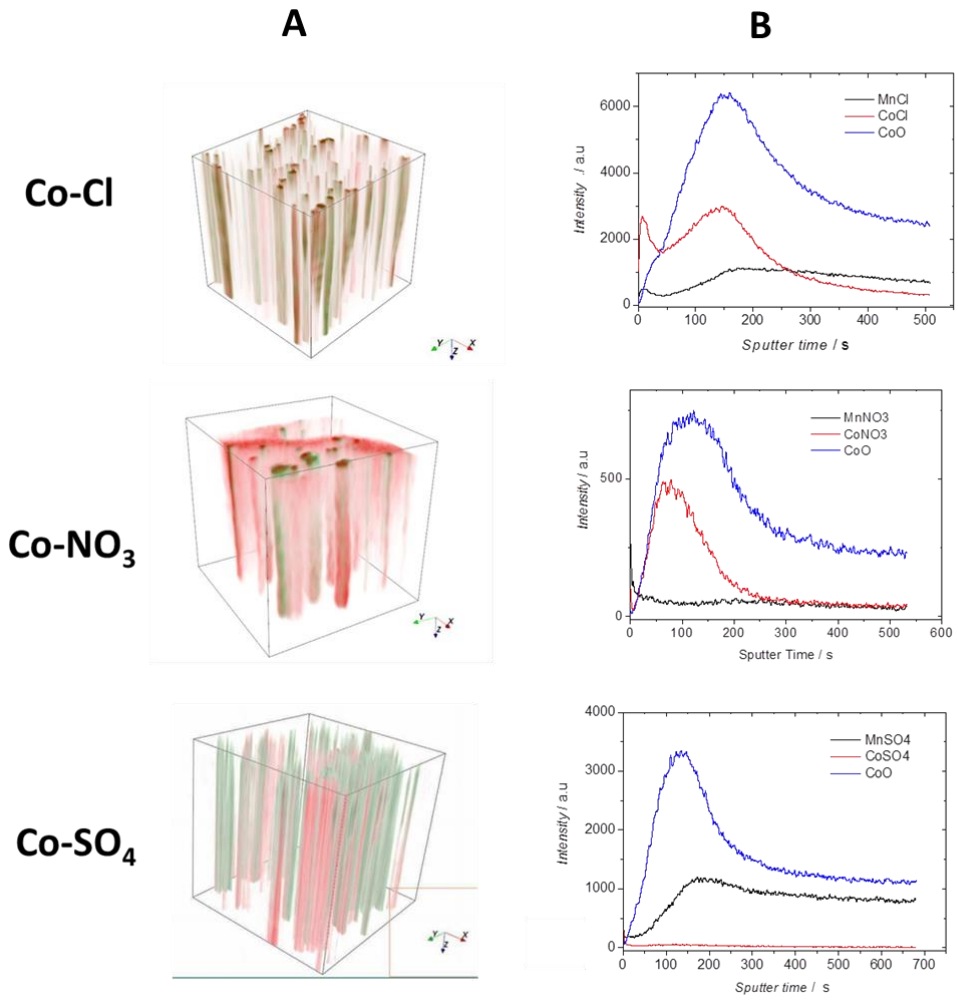

Figure 5. (A) ToF-SIMS positive ions 3D data reconstruction on the Co@KMO-Cl, Co@KMO-NO and Co@KMO-SO catalysts supported on glassy carbon. ToF-SIMS data were acquired using the CBA ("collimated, burst, alignment") mode.[39, 40] The 3D overlay images are reconstructed with the Co^+ fragments (m/z= 59) in green and the anion (Cl, NO_3 and SO_4) fragments in red respectively. Each system was acquired with a different field-of-view (FoV); 50×50 µm^2 for the Co@KMO-Cl and Co@KMO-SO systems and 20×20 µm^2 for the Co@KMO-NO system. (B) ToF-SIMS negative ions depth profiles using the spectrometry mode (high-current bunched mode) on the Co@KMO-Cl, Co@KMO-NO and Co@KMO-SO catalysts. Information about the acquisition and sputtering is given in the SI file.

Fig. S11 and S12 show the survey and fine-scan XPS spectra of Co modified samples. For the

Co 2p spectra, previous reports have shown that the separation of the peaks (Δ) associated to Co $2p_{3/2}$ and $2p_{1/2}$ can provide useful information of the electronic structure of the material. It has been suggested that the for high spin Co^{2+} the separation between the two peaks is 16.0 eV and for low spin Co^{3+} is 15.0 eV.[41, 42] The separation of the peaks for Co@KMO-Cl is 15.3 eV, whereas this separation for Co@KMO-NO and Co@KMO-SO is 15.0 eV. The oxidation state of Co on Co@KMO-Cl suggests that it has a lower oxidation state in comparison with the other two samples. The oxidation of Co on Co@KMO-Cl is accordance with the XAS analysis. Detailed deconvoluted spectra of the Co 2p with fits of $2p_{3/2.}$ are presented in **Fig. 6a**. The changed electronic structure can be attributed to the Cl incorporation, since the Mn shows identical chemical state of all Co modified samples (see *SI*). Partial Cl bonding with Co changes the electron density, leading the Co easily bonding with OH (as shown in the following O 1s spectra analysis). This result provides solid support to the formation of O…Co…Cl bonding (**Fig. S13**).

The detail XPS spectra of the O 1s convolution and fitting curves for the unmodified and Co-modified materials are presented in **Fig. 6b**. The band assigned to the lattice-O component (oxygen-metal interaction) shifted positively from 529.4 eV on KMO to 529.9 eV for all the Co-modified samples due to the new contribution of O-Co or the mixed interaction of O-Mn/O-Co. The branch at around 531.1 eV can be assigned to an OH contribution,[43] and this component increased markedly in all Co-modified samples while the lattice-O branch simultaneously decreased. It is important to notice that the highest gain was observed on the Co@KMO-Cl compared to Co@KMO-NO and Co@KMO-NO. This strongly suggests that the presence of Cl favours the adsorption of OH, which is the active phase towards the OER. The small convoluted peak at ~532.5 eV can be assigned to adventitious carbon contaminations.[44] **Fig. S14** displays the multiplet fitting curves of Mn $2p_{3/2}$ of KMO and Co@KMOs and the details of the fitting are presented in the

SI.

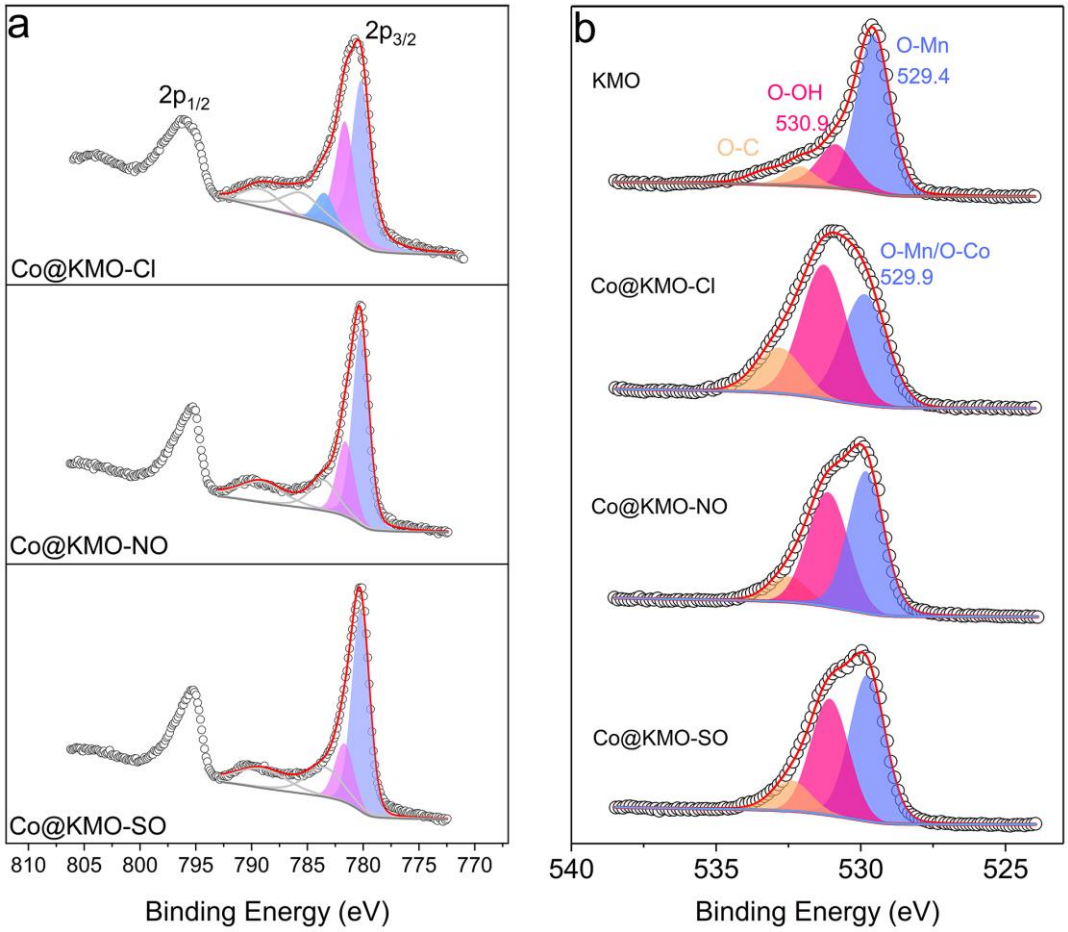

Figure 6. High resolution XPS spectra of different Co-modified KMOs: (a) Co 2p, (b) O 1s.

To systematically study the surface redox reaction taking place on KMO, Co@KMO-Cl samples were prepared in varying $CoCl_2$ concentrations. **Fig. S15-16** shows the SEM, TEM images of KMO modified with different $CoCl_2$ concentration (0.5 M, 0.25 M, 0.05 M and 0.01 M). It is clearly observed that the density of Co-OH nanoflakes on the surface is proportional to the $CoCl_2$ concentration. Thus, the electrochemically available surface area (ECSA) as a function of the concentration of chloride for the samples Co@KMO-$Cl_{0.5}$ and Co@KMO-$Cl_{0.01}$ were evaluated by measurement of the double layer capacitance as described in the *SI*. As shown in **Fig. S17**, the sample synthesized using a concentration of 0.5 M shows larger ECSA of 6.3-fold higher than that of 0.01 M.

The electronic structure of Co@KMO-$Cl_{0.5}$ and Co@KMO-$Cl_{0.01}$ were also investigated by XPS. As can be seen in **Fig. S18-20**, significantly weaker Cl signal was detected in Co@KMO-$Cl_{0.01}$. Correspondingly, the binding energies of Co 2p and O 1s were negatively shifted for Co@KMO-$Cl_{0.01}$ as compared to Co@KMO-$Cl_{0.5}$. The positions of the Mn 2p peaks remained unchanged, suggesting that the Cl ligand is bonded with Co, and thus has little effect on the Mn. As discussed above, incorporation of Cl led to positive shift of Co 2p and O 1s binding energy. This effect was weakened due to reduced Cl incorporation. XPS elements analysis in **Fig. S19** shown the ratio of Co/Cl of 0.24 in Co@KMO-$Cl_{0.5}$ and 0.07 in Co@KMO-$Cl_{0.01}$. Therefore, the tailoring effect of Cl on electronic structure was confirmed.

In summary, it was found that to the use different anions, Cl with similar ion radius and comparable electronegativity to oxygen, can participate in Co coordination, tailoring the electronic structure of Co and enhancing the interaction of OH with Co.

2.3 Assessment of the oxygen evolution reaction on Co@KMOs

The electrocatalytic performance and durability of Co@KMOs were evaluated in Ar-saturated 1 M NaOH solution using a rotating disk electrode (RDE). **Fig. 7a-c** show the comparison of the iR-corrected voltammetric profiles for all the Co@KMOs catalysts. The current density is reported as mA cm^{-2}, where the area is the geometric area of the electrode. All the Co@KMO catalysts are highly active towards the OER in contrast to the pristine KMO that does not show any catalytic activity as demonstrated in previous works.[27] Amongst all the catalysts prepared, Co@KMO-Cl exhibited the highest catalytic activity (η_{onset} = 170 mV, η_{10} = 245 mV). Co@KMO-NO displayed the second best performance (η_{onset} = 220 mV, η_{10} = 338 mV) and Co@KMO-SO the lowest catalytic activity (η_{onset} = 230 mV, η_{10} = 377 mV).

A close look at the potential window between 0.9 and 1.5 V vs RHE, **(Fig. 7b)** shows a large increase in the double layer capacity of the Co@KMO voltammograms. This increase is largest for the Co@KMO-Cl sample, which might be indicative of differences in the surface area. Common practice in the literature is the utilization of the double layer capacity to determine the electrochemical surface area of metal oxide catalysts, however this electrochemical double-layer capacitance-based method involves empiric assumptions, which are certainly inaccurate.[45, 46] A more tangible method of comparison of electrocatalyst is the normalization per mass of the active center, which in the case of this work is the mass of cobalt. In order to be able to provide a result that enables us to compare the catalytic activity of our catalyst with other reports in the literature we provide the catalytic activity using both methods: *i)* normalization per ECSA and *ii)* normalization per mass of Co. The determination of the ECSA based on the double layer capacitance (C_{dl}) is described in the *SI*[13] and the results presented on **Fig. S21**. The largest increase in C_{dl} and thus, ECSA, was found for the Co@KMO-Cl compared to that for Co@KMO-NO and Co@KMO-SO. Such an increase of the ECSA can be associated with the different material morphologies described above (see HRTEM **Fig. 2b, g**).

The mass activity normalized by Co loading and the ECSA-normalized curves of Co@KMOs are shown in **Fig. S22**. As can be seen, the catalytic activity of the Co@KMO-Cl is larger than the catalytic activity of the Co@KMO-NO and Co@KMO-SO independent of the normalization method. Considering that our primary figure of benchmarking the catalyst against those in the literature is the overpotential required to achieve a current density ECSA at 10 mA cm^{-2}, the catalytic activity of the Co@KMO-Cl is comparable or better than the non-precious metals state-of-art catalysts for the OER in alkaline media (**Table S7)**.

In order to get more insight regarding the kinetics of the reaction and the rate determine step

(RDS), the Tafel slopes were extracted for all the samples (**Fig. 7d)**. The smallest Tafel slope (faster kinetics) was found for the Co@KMO-Cl (42 mV dec^{-1}); while the values of Co@KMO-NO and Co@KMO-SO are 63 and 71 mV dec^{-1}, respectively. The proposed proton-coupled electron-transfer mechanism (water nucleophilic attack) for the OER in alkaline media on Co catalyst is as follows:[47, 48]

$$Co^{*} + OH^{-} \rightarrow Co^{*}OH + e^{-} \quad (2)$$

$$Co^{*}OH + OH^{-} \rightarrow Co^{*}O + H_2O + e^{-} \quad (3)$$

$$Co^{*}O + OH^{-} \rightarrow Co^{*}OOH + e^{-} \quad (4)$$

$$Co^{*}OOH + OH^{-} \rightarrow Co^{*} + O_2 + H_2O + e^{-} \quad (5)$$

Based on the values of the Tafel Slope, we propose the RDS of the OER for the Cl-containing sample is the second electron transfer step (**Eq. 3**, a theoretical value of 40 mV dec^{-1}). On the other hand, Tafel slopes of 60 mV dec^{-1} observed on the Co@KMO-NO and Co@KMO-SO samples, suggest a change of the reaction mechanism. In this case, **Eq. 3** can be written as nonconcerted proton-electron steps [49, 50]:

$Co^{*}OH + OH^{-} \rightarrow Co^{*}O^{-} + H_2O +$

$Co^{*}O^{-} \rightarrow Co^{*}O + e^{-}$

In this case, the RDS is associated to the deprotonation step of $Co^{*}OH$ to $Co^{*}O^{-}$, which occurs prior to the second electron transfer. As shown in **Fig. 6**, the electronic structure of Co@KMO-Cl was tailored by the presence of Cl. The positively shifted Co 2p binding energy and the enhancement of OH adsorption on Co@KMO-Cl suggest favorable interaction of the OH^{-} reactant with active sites, which moved the RDS to second electron transfer step. This effect on Co@KMO-Cl can be also associated with the negatively shifted OER onset potential, where the adsorption step has finished and subsequent electron-proton step is initialized.[50, 51] Furthermore, A possible explanation for the higher catalytic activity of the chloride containing samples can be linked to the presence of a higher density of defects on the surface of the catalyst as a results of the etching of cobalt hydroxides by chloride ions.[52]

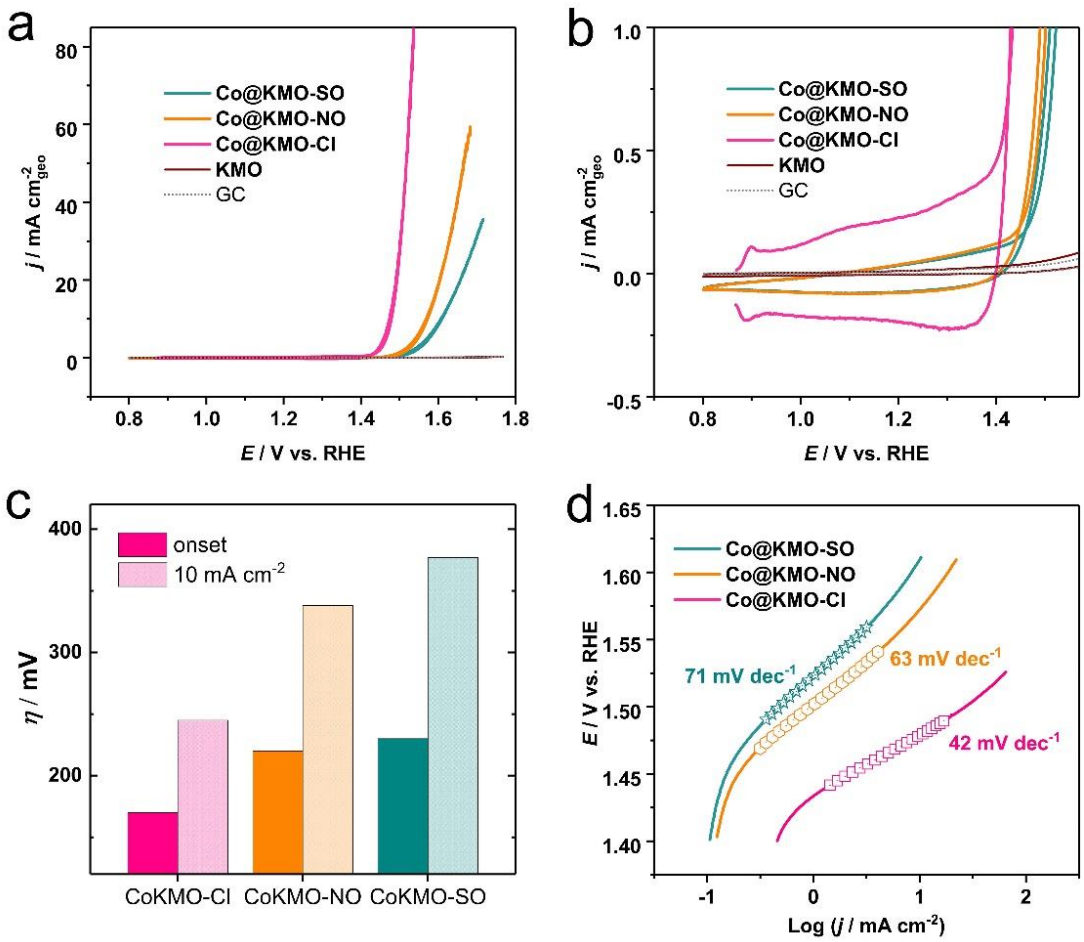

Figure 7. (**a**) Stable cyclic voltammograms of Co salts reacted Co@KMO at pH=14 after 10 consecutive scans in NaOH electrolyte, with scan rate of 20 mV s^{-1}. The profile of the glassy carbon (GC) support is included for comparison. All the curves are iR-corrected. **(b)** Enlarged region showing the double layer region of various Co@KMO. (**c**) The onset overpotential (η_{onset}) and overpotential at j = 10 mA cm^{-2} (η_{10}) obtained from (a). (**d**) Tafel slopes for the OER on the Co@KMO catalyst prepared with different anions.

Fig. 8 shows the voltammograms and Tafel plots of the OER on the Co@KMO-Cl prepared with different concentration of $CoCl_2$ precursor. When normalized by the geometrical area, the catalytic activity of the OER increases as the concentration of $CoCl_2$ used in the preparation of Co@KMO-Cl increases from 0.01 M $CoCl_2$ to 0.5 M $CoCl_2$. Thus, we assume that the activity is directly controlled by the Co-OH species generated on the surface due to the increase in

concentration of the $CoCl_2$ precursor. To confirm this assumption, the loading of Co on the catalyst as a function of the concentration of the precursors was determine by XRF (**Fig. S23**) and the mass activity (normalized by the Co loading) is shown on **Fig. 8a**. It is evident that higher Co loading resulted in higher mass activity, following the same trend observed for geometrical activity. A higher catalytic activity was observed on the Co@KMO-$Cl_{0.5}$, which only requires an overpotential of 230 mV to reach 50 mA g_{Co}^{-1}.

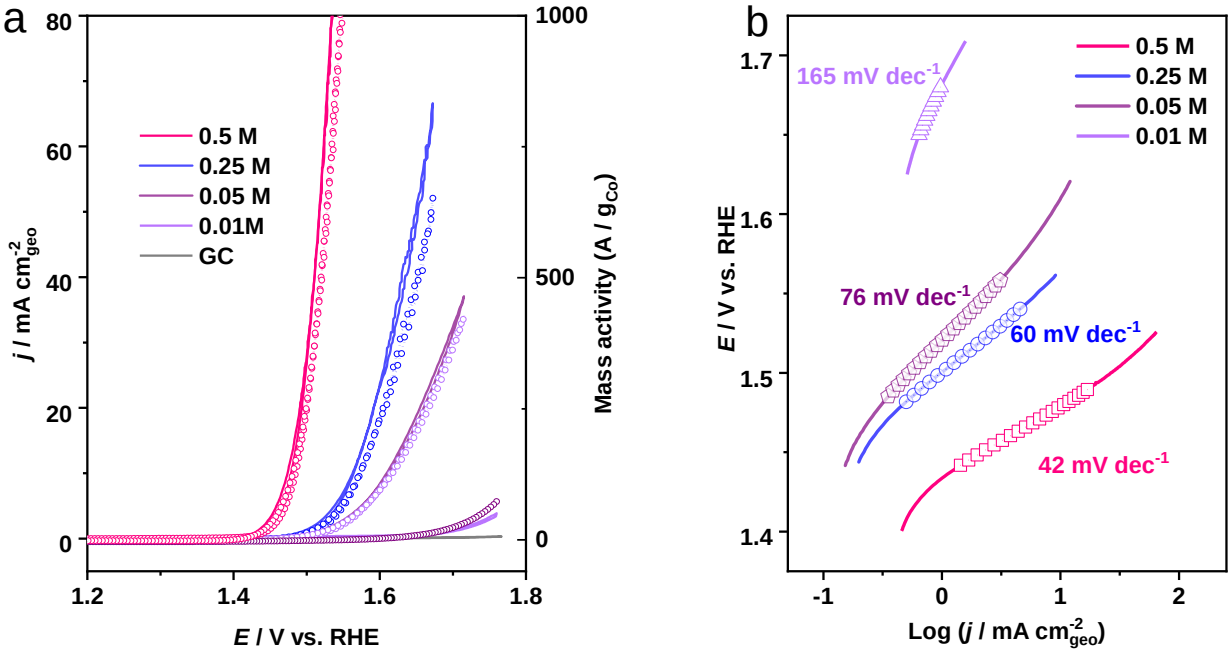

Figure 8. (a) Stable cyclic voltammograms in 1 M NaOH solution of Co@KMO-Cl samples synthesized with different concentration of $CoCl_2$ as indicated in different color, solid lines (left Y axis): geometrical activity; (◦) symbols (right Y axis): mass activity. The stable voltammogram was recorded after 10 consecutive scans. The voltammogram of the glassy carbon (GC) support is included for comparison. All the curves are iR-corrected. Scan rate υ= 20 mV s^{-1}. **(b)** corresponding Tafel plots in the potential range between 1.4 and 1.7 V vs RHE.

2.4 Long term stability of Co@KMOs during the oxygen evolution reaction

The long-term stability also plays a pivotal role in the evaluation of an electrocatalyst, especially for commercial applications. Fig. 9a shows the electrolysis in a 1 M NaOH solution at 1.48 V vs. RHE for 22 h using the Co@KMO-$Cl_{0.5}$ as electrocatalyst. The chronoamperometric curve shows stable $j \approx 10$ mA cm^{-2} during the total duration of the experiment. HR-TEM and cyclic voltammetry of the catalyst before and after the electrolysis were recorded in order to determine any changes or degradation of the catalyst over time. HR-TEM image of Co@KMO-$Cl_{0.5}$ after 22 h electrolysis shows transformation of the edge of the Co-OH nanoflakes from a more crystalline structure (**Fig. 9b**) to a more amorphous one (**Fig. 9c**). Such changes during OER process have been previously reported and have been associated to oxidation state evolution of active sites and its coordinations.[53-55] Even though, structural changes were observed on the electron microscopy, the cyclic voltammograms of the Co@KMO-Cl before and after the electrolysis show negligible differences (**Fig. S24**). No additional signals were found in the Raman spectra on Co@KMO-Cl after a long-term stability test, while slight change in peak intensity of 578 cm^{-1} clearly demonstrated the surface reconstruction, as observed in TEM image. In order to confirm whether the changes of the morphology of the catalyst changed at the start of the reaction or during the whole chronoamperometry, high resolution SEM images where obtained after 10 cycles between 0.8 and 1.5 V (**Fig. S25**). It was observed that structure of the catalyst changed at very early stages of the reaction. Thus, after the formation of this reconstructed morphology, the catalyst is stable not only in terms of catalyst activity but also the morphology of the matrix. Despite of the local surface reconstruction, the identical phase structure (**Fig. S26**) and homogenous element distribution visualized by SEM-EDS (**Fig. S27**) confirm the observed stability.

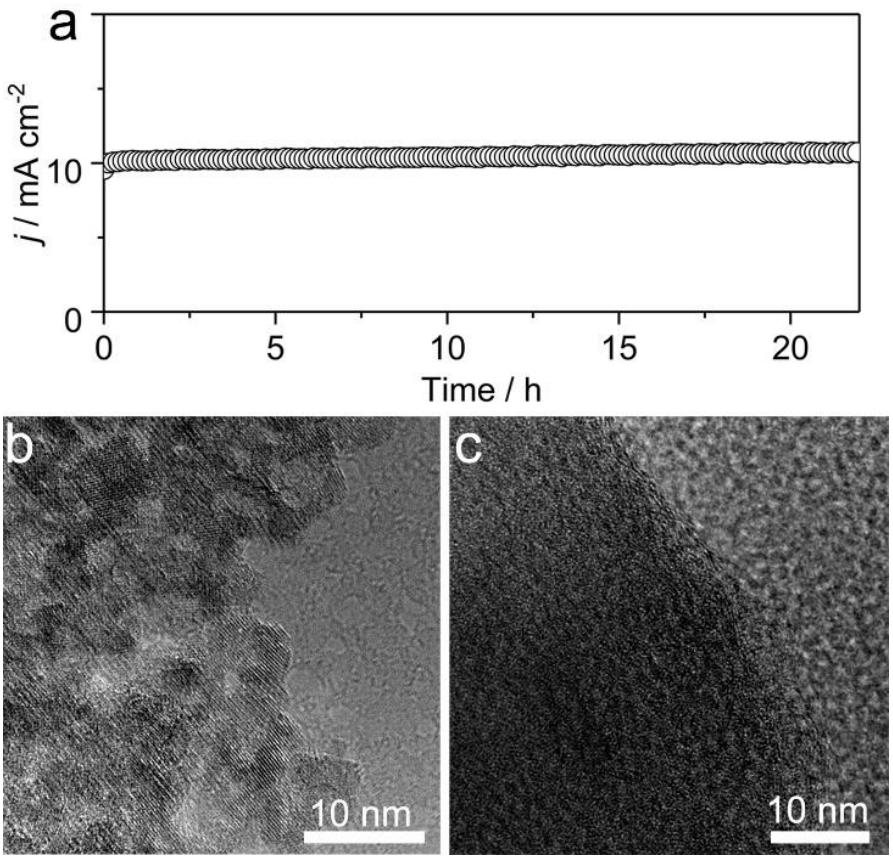

Figure 9. (a) 24 h chronoamperometry profile of Co@KMO-$Cl_{0.5}$ at 1.48 V vs. RHE in 1 M NaOH solution. HR-TEM images of Co@KMO-$Cl_{0.5}$ (b) before, and (c) after electrolysis.

3. **Conclusion**

In this work, we demonstrated that surface galvanic formation of Co-OH on Birnessite is a clean, green route for the design of highly efficient catalysts for OER. This simple method provides a route for the synthesis of ultrathin and high surface area CoOOH nanosheets with 3-4 nm thickness supported on KMO. The simple and clean synthesis method involves the surface redox reaction of hydrated Co^{2+} and crystalline Mn^{4+} at ambient temperature, without use of additional surfactants or capping materials. Thus, the resulting catalyst can be implemented directly as catalyst without extra cleaning or high-temperature steps.

X-ray adsorption spectroscopy (XAS) and X-ray photoelectron spectroscopy (XPS) analysis confirmed the changes in the oxidation state of the bulk and surface species $Co^{+2} \rightarrow Co^{+2.75}$ and $Mn^{+3.9} \rightarrow Mn^{+3.1}$. The effect of the anions, on the Co precursor, $CoCl_2$, $Co(NO_3)_2$ and $CoSO_4$

was evaluated. It was found that the use of different anions in the preparation of the catalyst results in changes to the coordination chemistry and electronic structure of the catalyst. These changes influenced the activity of the catalyst with Co@KMO-Cl being identified as the most active for OER compared to the Co@KMO-NO and Co@KMO-SO catalysts. The presence of Cl was found to favor the formation of Co-OH. Further, The kinetic analysis suggests that such an increase in the catalytic activity on the Co@KMO-Cl is due to the change of the RDS from the OH adsorption step to the coupled electron-deprotonation step instead. The Co@KMO-Cl showed improved catalytic activity in comparison with non-precious metal state-of-the-art catalyst for the OER in alkaline media with an overvoltage of only 245 mV to achieve 10 mA cm_{geo}^{-2} (Table S7). Long-term stability tests demonstrated that the Co@KMO-Cl has an excellent stability by showing steady current density during the OER for at least 20 h.

4. Supporting information

The Supporting Information is available free of charge on the xxxxxxx website at DOI:

5. Acknowledgment

This work was financially supported by Southern University of Science and Technology (SUSTech) start fund through Shenzhen Peacock Talent program, the Basic Research Fund of Shenzhen (JCYJ20150507170334573), and Guangdong Innovative and Entrepreneurial Research Team Program (No.2016ZT06N532). P.R. acknowledges the University of Birmingham for financial support through the Birmingham fellowship program and the travel fund to perform experiments at BAM. TEM, Raman data were obtained using equipment maintained by Southern

University of Science and Technology Core Research Facilities. The authors wish to acknowledge the Diamond Light Source for provision of beamtime (SP21659 and SP19850).

6. Authors contributions

YP, PR and LH conceived the experiments. YP performed the experiments and analyses the data. EXAFS characterization and analyses were performed by VC, ML and AER. XES data were collected and analyzed by VC and AER. STEM characterization was performed by WW and ZS. JMS and JR performed the XPS experiments in BAM and OS performed the ToF-SIMS experiments at BAM. All authors contributed to the analysis of the results, discussion, writing and revision of the manuscript. All authors have given approval to the final version of the manuscript.

7. References

[1] Z.W. Seh, J. Kibsgaard, C.F. Dickens, I. Chorkendorff, J.K. Nørskov, T.F. Jaramillo, Combining theory and experiment in electrocatalysis: Insights into materials design, Science, 355 (2017).

[2] D.A. Kuznetsov, B. Han, Y. Yu, R.R. Rao, J. Hwang, Y. Román-Leshkov, Y. Shao-Horn, Tuning redox transitions via inductive effect in metal oxides and complexes, and implications in oxygen electrocatalysis, Joule, 2 (2018) 225-244.

[3] C. Spoeri, J.T.H. Kwan, A. Bonakdarpour, D.P. Wilkinson, P. Strasser, The stability challenges of oxygen evolving catalysts: towards a common fundamental understanding and mitigation of catalyst degradation, Angewandte Chemie International Edition, 56 (2017) 5994-6021.

[4] J.H. Montoya, L.C. Seitz, P. Chakthranont, A. Vojvodic, T.F. Jaramillo, J.K. Nørskov, Materials for solar fuels and chemicals, Nature Materials, 16 (2017) 70-81.

[5] M.T. Koper, Volcano activity relationships for proton-coupled electron transfer reactions in electrocatalysis, Topics in Catalysis, 58 (2015) 1153-1158.

[6] L.C. Seitz, C.F. Dickens, K. Nishio, Y. Hikita, J. Montoya, A. Doyle, C. Kirk, A. Vojvodic, H.Y.

Hwang, J.K. Norskov, A highly active and stable IrOx/SrIrO3 catalyst for the oxygen evolution reaction, Science, 353 (2016) 1011-1014.

[7] P.C. Vesborg, T.F. Jaramillo, Addressing the terawatt challenge: scalability in the supply of chemical elements for renewable energy, Rsc Advances, 2 (2012) 7933-7947.

[8] B.M. Hunter, H.B. Gray, A.M. Müller, Earth-Abundant Heterogeneous Water Oxidation Catalysts, Chemical Reviews, 116 (2016) 14120-14136.

[9] J.O.M. Bockris, Kinetics of activation controlled consecutive electrochemical reactions: anodic evolution of oxygen, The Journal of Chemical Physics, 24 (1956) 817-827.

[10] A.C.C. Tseung, S. Jasem, Oxygen evolution on semiconducting oxides, Electrochimica Acta, 22 (1977) 31-34.

[11] J.O.M. Bockris, T. Otagawa, Mechanism of oxygen evolution on perovskites, The Journal of Physical Chemistry, 87 (1983) 2960-2971.

[12] S.I. Córdoba, R.E. Carbonio, M.L. Teijelo, V.A. Macagno, The effect of iron hydroxide on nickelous hydroxide electrodes with emphasis on the oxygen evolution reaction, Electrochimica Acta, 32 (1987) 749-755.

[13] C.C.L. McCrory, S. Jung, J.C. Peters, T.F. Jaramillo, Benchmarking Heterogeneous Electrocatalysts for the Oxygen Evolution Reaction, Journal of the American Chemical Society, 135 (2013) 16977-16987.

[14] W.T. Hong, M. Risch, K.A. Stoerzinger, A. Grimaud, J. Suntivich, Y. Shao-Horn, Toward the rational design of non-precious transition metal oxides for oxygen electrocatalysis, Energy & Environmental Science, 8 (2015) 1404-1427.

[15] F. Song, X. Hu, Ultrathin cobalt–manganese layered double hydroxide is an efficient oxygen evolution catalyst, Journal of the American Chemical Society, 136 (2014) 16481-16484.

[16] F. Song, M.M. Busch, B. Lassalle-Kaiser, C.-S. Hsu, E. Petkucheva, M. Bensimon, H.M. Chen, C. Corminboeuf, X. Hu, An Unconventional Iron Nickel Catalyst for the Oxygen Evolution Reaction, ACS Central Science, 5 (2019) 558-568.

[17] J. Zhang, J. Liu, L. Xi, Y. Yu, N. Chen, S. Sun, W. Wang, K.M. Lange, B. Zhang, Single-Atom Au/NiFe Layered Double Hydroxide Electrocatalyst: Probing the Origin of Activity for Oxygen Evolution Reaction, Journal of the American Chemical Society, 140 (2018) 3876-3879.

[18] G. Chen, Y. Zhu, H.M. Chen, Z. Hu, S.-F. Hung, N. Ma, J. Dai, H.-J. Lin, C.-T. Chen, W. Zhou, Z. Shao, An Amorphous Nickel–Iron-Based Electrocatalyst with Unusual Local Structures for Ultrafast Oxygen Evolution Reaction, Advanced Materials, 31 (2019) 1900883.

[19] M.W. Louie, A.T. Bell, An investigation of thin-film Ni–Fe oxide catalysts for the electrochemical evolution of oxygen, Journal of the American Chemical Society, 135 (2013) 12329-12337.

[20] O. Diaz-Morales, I. Ledezma-Yanez, M.T. Koper, F. Calle-Vallejo, Guidelines for the rational design of Ni-based double hydroxide electrocatalysts for the oxygen evolution reaction, ACS Catalysis, 5 (2015) 5380-5387.

[21] M.J. Lawrence, V. Celorrio, X. Shi, Q. Wang, A. Yanson, N.J.E. Adkins, M. Gu, J. Rodríguez-López, P. Rodriguez, Electrochemical Synthesis of Nanostructured Metal-Doped Titanates and Investigation of Their Activity as Oxygen Evolution Photoanodes, ACS Applied Energy Materials, 1 (2018) 5233-5244.

[22] J. Guan, Z. Duan, F. Zhang, S.D. Kelly, R. Si, M. Dupuis, Q. Huang, J.Q. Chen, C. Tang, C. Li, Water oxidation on a mononuclear manganese heterogeneous catalyst, Nature Catalysis, 1 (2018) 870.

[23] L.S. Balistrieri, J.W. Murray, The surface chemistry of sediments from the Panama Basin: The influence of Mn oxides on metal adsorption, Geochimica et Cosmochimica Acta, 50 (1986) 2235-2243.

[24] A. Manceau, E. Silvester, C. Bartoli, B. Lanson, V.A. Drits, Structural mechanism of Co2+ oxidation by the phyllomanganate buserite, American mineralogist, 82 (1997) 1150-1175.

[25] A.C. Thenuwara, E.B. Cerkez, S.L. Shumlas, N.H. Attanayake, I.G. McKendry, L. Frazer, E. Borguet, Q. Kang, R.C. Remsing, M.L. Klein, Nickel confined in the interlayer region of birnessite: an active electrocatalyst for water oxidation, Angewandte Chemie, 128 (2016) 10537-10541.

[26] A.C. Thenuwara, S.L. Shumlas, N.H. Attanayake, Y.V. Aulin, I.G. McKendry, Q. Qiao, Y. Zhu, E. Borguet, M.J. Zdilla, D.R. Strongin, Intercalation of cobalt into the interlayer of birnessite improves oxygen evolution catalysis, ACS Catalysis, 6 (2016) 7739-7743.

[27] Y. Pu, M.J. Lawrence, V. Celorrio, Q. Wang, M. Gu, Z. Sun, L.A. Jácome, A.E. Russell, L. Huang, P. Rodriguez, Nickel confined in 2D earth-abundant oxide layers for highly efficient and durable oxygen evolution catalysts, Journal of Materials Chemistry A, 8 (2020) 13340-13350.

[28] C. Julien, M. Massot, R. Baddour-Hadjean, S. Franger, S. Bach, J. Pereira-Ramos, Raman spectra of birnessite manganese dioxides, Solid State Ionics, 159 (2003) 345-356.

[29] C.M. Julien, M. Massot, C. Poinsignon, Lattice vibrations of manganese oxides: Part I. Periodic structures, Spectrochimica Acta Part A: Molecular and Biomolecular Spectroscopy, 60 (2004) 689-700.

[30] H. An, Z. Chen, J. Yang, Z. Feng, X. Wang, F. Fan, C. Li, An Operando-Raman study on oxygen evolution of manganese oxides: Roles of phase composition and amorphization, Journal of catalysis, 367 (2018) 53-61.

[31] T. Pauporté, L. Mendoza, M. Cassir, M.C. Bernard, J. Chivot, Direct Low-Temperature Deposition of Crystallized CoOOH Films by Potentiostatic Electrolysis, Journal of The Electrochemical Society, 152 (2005) C49.

[32] J. Yang, H. Liu, W.N. Martens, R.L. Frost, Synthesis and Characterization of Cobalt Hydroxide, Cobalt Oxyhydroxide, and Cobalt Oxide Nanodiscs, The Journal of Physical Chemistry C, 114 (2010) 111-119.

[33] M.C. Militello, S.J. Simko, Palladium chloride (PdCl2) by XPS, Surface Science Spectra, 3 (1994) 402-409.

[34] H. Jiang, Q. He, X. Li, X. Su, Y. Zhang, S. Chen, S. Zhang, G. Zhang, J. Jiang, Y. Luo, P.M. Ajayan, L. Song, Tracking Structural Self-Reconstruction and Identifying True Active Sites toward Cobalt Oxychloride Precatalyst of Oxygen Evolution Reaction, Advanced Materials, 31 (2019) 1805127.

[35] J. Suntivich, K.J. May, H.A. Gasteiger, J.B. Goodenough, Y. Shao-Horn, A Perovskite Oxide Optimized for Oxygen Evolution Catalysis from Molecular Orbital Principles, Science, 334 (2011) 1383-1385.

[36] E. Ahmad, G. Mallia, D. Kramer, V. Tileli, A. Kucernak, N. Harrison, Comment on “2D Atomic Mapping of Oxidation States in Transition Metal Oxides by Scanning Transmission Electron Microscopy and Electron Energy-Loss Spectroscopy”, Physical review letters, 108 (2012) 259701.

[37] A. Ignatov, S. Khalid, R. Sujoy, N. Ali, Theoretical study of Mn K-edge in La1-xCaxMnO3, Journal of synchrotron radiation, 8 (2001) 898-900.

[38] J. Chaboy, Relationship between the structural distortion and the Mn electronic state in La1−

xCaxMnO3: a Mn K-edge XANES study, Journal of synchrotron radiation, 16 (2009) 533-544.

[39] G. Holzlechner, M. Kubicek, H. Hutter, J. Fleig, A novel ToF-SIMS operation mode for improved accuracy and lateral resolution of oxygen isotope measurements on oxides, Journal of Analytical Atomic Spectrometry, 28 (2013) 1080-1089.

[40] M. Kubicek, G. Holzlechner, A.K. Opitz, S. Larisegger, H. Hutter, J. Fleig, A novel ToF-SIMS operation mode for sub 100 nm lateral resolution: Application and performance, Appl Surf Sci, 289 (2014) 407-416.

[41] P.W. Menezes, A. Indra, A. Bergmann, P. Chernev, C. Walter, H. Dau, P. Strasser, M. Driess, Uncovering the prominent role of metal ions in octahedral versus tetrahedral sites of cobalt–zinc oxide catalysts for efficient oxidation of water, Journal of Materials Chemistry A, 4 (2016) 10014-10022.

[42] M. Oku, K. Hirokawa, X-ray photoelectron spectroscopy of Co3O4, Fe3O4, Mn3O4, and related compounds, Journal of Electron Spectroscopy and Related Phenomena, 8 (1976) 475-481.

[43] Z.-F. Huang, J. Song, Y. Du, S. Xi, S. Dou, J.M.V. Nsanzimana, C. Wang, Z.J. Xu, X. Wang, Chemical and structural origin of lattice oxygen oxidation in Co–Zn oxyhydroxide oxygen evolution electrocatalysts, Nature Energy, 4 (2019) 329-338.

[44] J. Stoch, J. Gablankowska-Kukucz, The effect of carbonate contaminations on the XPS O 1s band structure in metal oxides, Surface and Interface Analysis, 17 (1991) 165-167.

[45] T. Bligaard, R.M. Bullock, C.T. Campbell, J.G. Chen, B.C. Gates, R.J. Gorte, C.W. Jones, W.D. Jones, J.R. Kitchin, S.L. Scott, Toward Benchmarking in Catalysis Science: Best Practices, Challenges, and Opportunities, ACS Catalysis, 6 (2016) 2590-2602.

[46] J.G. Chen, C.W. Jones, S. Linic, V.R. Stamenkovic, Best Practices in Pursuit of Topics in Heterogeneous Electrocatalysis, ACS Catalysis, 7 (2017) 6392-6393.

[47] H. Dau, C. Limberg, T. Reier, M. Risch, S. Roggan, P. Strasser, The Mechanism of Water Oxidation: From Electrolysis via Homogeneous to Biological Catalysis, ChemCatChem, 2 (2010) 724-761.

[48] J. Hessels, R.J. Detz, M.T.M. Koper, J.N.H. Reek, Rational Design Rules for Molecular Water Oxidation Catalysts based on Scaling Relationships, Chemistry – A European Journal, 23 (2017) 16413-16418.

[49] M.S. Burke, M.G. Kast, L. Trotochaud, A.M. Smith, S.W. Boettcher, Cobalt–Iron (Oxy)hydroxide Oxygen Evolution Electrocatalysts: The Role of Structure and Composition on Activity, Stability, and Mechanism, Journal of the American Chemical Society, 137 (2015) 3638-3648.

[50] Y. Surendranath, M.W. Kanan, D.G. Nocera, Mechanistic Studies of the Oxygen Evolution Reaction by a Cobalt-Phosphate Catalyst at Neutral pH, Journal of the American Chemical Society, 132 (2010) 16501-16509.

[51] B.S. Yeo, A.T. Bell, Enhanced Activity of Gold-Supported Cobalt Oxide for the Electrochemical Evolution of Oxygen, Journal of the American Chemical Society, 133 (2011) 5587-5593.

[52] P.F. Liu, S. Yang, L.R. Zheng, B. Zhang, H.G. Yang, Electrochemical etching of α-cobalt hydroxide for improvement of oxygen evolution reaction, Journal of Materials Chemistry A, 4 (2016) 9578-9584.

[53] N. Ortiz Peña, D. Ihiawakrim, M. Han, B. Lassalle-Kaiser, S. Carenco, C. Sanchez, C. Laberty-Robert, D. Portehault, O. Ersen, Morphological and Structural Evolution of Co3O4 Nanoparticles Revealed by in Situ Electrochemical Transmission Electron Microscopy during Electrocatalytic Water Oxidation, ACS Nano, 13 (2019) 11372-11381.

[54] A. Grimaud, K.J. May, C.E. Carlton, Y.-L. Lee, M. Risch, W.T. Hong, J. Zhou, Y. Shao-Horn, Double perovskites as a family of highly active catalysts for oxygen evolution in alkaline solution, Nature Communications, 4 (2013) 2439.

[55] Z. Chen, L. Cai, X. Yang, C. Kronawitter, L. Guo, S. Shen, B.E. Koel, Reversible Structural Evolution of NiCoOxHy during the Oxygen Evolution Reaction and Identification of the Catalytically Active Phase, ACS Catalysis, 8 (2018) 1238-1247.